

**EXPERIMENTAL INVESTIGATIONS INTO THERMAL PULSATILE BOUNDARY  
LAYER FLOW**

BY

DRUMMOND BILES

BS, Mechanical Engineering, University of New Hampshire, New Hampshire, 2013

DISSERTATION

Submitted to the University of New Hampshire  
in Partial Fulfillment of  
the Requirements for the Degree of

Doctor of Philosophy

in

Mechanical Engineering

May 2019

ALL RIGHTS RESERVED

©2015

Drummond Biles

This dissertation has been examined and approved in partial fulfillment of the requirements for the degree of Doctor of Philosophy in Mechanical Engineering by:

**Dissertation Director, Christopher White,**  
Associate Professor of Mechanical Engineering

**Gregory P. Chini,**  
Professor of Integrated Applied Mathematics  
and Mechanical Engineering

**Yves Dubief,**  
Associate Professor of Mechanical Engineering

**Joeseph Klewicki,**  
Professor of Mechanical Engineering

**Martin Wosnik,**  
Associate Professor of Mechanical Engineering

on 05/19/2019.

Original approval signatures are on file with the University of New Hampshire Graduate School.

*This thesis decicated to someone.*

## **ACKNOWLEDGMENTS**

people

## TABLE OF CONTENTS

	<b>Page</b>
<b>ACKNOWLEDGMENTS</b> .....	v
<b>NOMENCLATURE</b> .....	viii
<b>LIST OF TABLES</b> .....	viii
<b>LIST OF FIGURES</b> .....	ix
<b>ABSTRACT</b> .....	xii
 <b>CHAPTER</b>	
<b>1. INTRODUCTION</b> .....	<b>1</b>
1.1 Boundary Layers .....	2
1.2 Thermal Boundary Layers .....	2
1.3 Non-Equilibrium Boundary Layers .....	2
1.4 Experimental Investigations .....	2
<b>2. THEORY</b> .....	<b>7</b>
2.1 Boundary Layers .....	7
2.2 Reynolds Analogy .....	7
2.3 Non-equilibrium Flow .....	8
2.4 Determination of Wall Heat Flux .....	8
<b>3. EXPERIMENTAL METHODS</b> .....	<b>11</b>
3.1 Velocity Measurements .....	11
3.2 Thermal Measurements .....	11
<b>4. NEAT BOUNDARY LAYER WIND TUNNEL</b> .....	<b>13</b>
4.1 Experimental Facility .....	13
4.1.1 General Description.....	13

4.1.2	Inlet Section .....	14
4.1.3	Test Section .....	16
4.2	Thermal Wall-plate .....	17
4.2.1	Prototype Wall-plate .....	17
4.2.2	Finalized Wall-plate .....	19
4.3	Pulsatile Flow Generator .....	22
4.3.1	Rotor-Stator Assembly .....	22
4.3.2	Pulsatile Flow Generator .....	24
<b>5.</b>	<b>RESULTS AND DISCUSSION .....</b>	<b>25</b>
5.1	Validation Tests .....	25
5.1.1	ZPG turbulent boundary layer flow over an isothermal wall plate .....	25
5.1.2	ZPG boundary layer encountering a sharp step in wall temperature .....	28
5.1.3	ZPG turbulent boundary layer flow around a wall mounted hemisphere body .....	31
5.2	Non-equilibrium Flow .....	34
5.3	Modified Correlations .....	34
<b>6.</b>	<b>CONCLUSION .....</b>	<b>35</b>
<b>BIBLIOGRAPHY .....</b>		<b>36</b>
<b>APPENDICES</b>		
<b>A.</b>	<b>DRAWINGS .....</b>	<b>37</b>
<b>B.</b>	<b>COMPONENTS .....</b>	<b>38</b>
<b>C.</b>	<b>MORE EXTRA STUFF .....</b>	<b>41</b>

## LIST OF TABLES

<b>Table</b>		<b>Page</b>
4.1	The length of the convective plates. Plate 1 is at the upstream end and plate 12 is at the downstream end of the wind tunnel. ....	21
5.1	Parameters for measured temperature profiles .....	27

## LIST OF FIGURES

<b>Figure</b>		<b>Page</b>
4.1	Schematic of the experimental facility. Air enters the facility from right-to-left. The primary components include: (1) freestream heaters, (2) seeding manifold, (3) turbulence management section, (4) contraction, (5) thermal wall-plate located on the bottom wall of the test-section, (6) rotor-stator assembly, (7) diffuser, (8) centrifugal fan. ....	13
4.2	(a) Probability density function (PDF) of freestream temperature measured in the wind tunnel over a two hour period. The vertical green line represents the setpoint temperature and the vertical red line represents the measured mean temperature with a confidence interval of 99%. (b) Schematic of the seeding manifold used for particle image velocimetry (PIV). ....	15
4.3	Schematic of removable windows which allow for optical measurements and installation of temperature/velocity probes. Design was developed by Dr. Michael Allard .....	17
4.4	Solid model of prototype thermal wall plate with two convective plates. ....	18
4.5	(a) Solid model schematic of the thermal wall-plate. (b) Detailed schematic of a section of the thermal wall-plate: right tilted $45^\circ$ lines denotes the heated wall plate, left tilted $45^\circ$ lines shows the surrounding layer of calcium silicate insulation and the hash marked section represents the co-polymer acetal frame which positions all components. Three evenly spaced embedded thermocouples are located along line AA. ....	20
4.6	(a) Image of roughing pass for the fabrication of the super-ellipse leading edge nose of the wall plate (b) final image of leading edge frame component for the wall plate .....	21
4.7	A diagram detailing the wall plate heater controller circuit. (1) designates the embedded thermocouples, which are fed to an amplifier (3), whose signal is then fed to a LabVIEW program (2), which determines if the heaters should be in an off or on position and sends a final signal to an SCR circuit (4), which communicates to the thermal wallplate heaters. ....	22
4.8	Schematic of rotor-stator design, left shows the rotor, shown in the middle is the stator, and the right plot depicts a freestream velocity time series taken with a pitot-static tube for a quarter revolution of the rotor-stator mechanism.....	23

4.9	Schematic of pulsatile wave generator with a paddle design. The left image displays the y-z plane with flow going into the board, where the right figure shows a cutaway image with paddle height $H_p$ . $H_p$ can be adjusted for desired flow condition. . . . .	24
5.1	(a) Representative ensemble-averaged IR image of plate #5 for $T_{set} = 40^\circ\text{C}$ . (b) Spanwise profile of streamwise averaged temperature from figure (a). . . . .	25
5.2	Wall-normal profiles of mean streamwise velocity at $Re_\theta = 1527$ with thermal wall plate on ( $\times$ ) and off ( $\triangleleft$ ) plotted in (a) outer-coordinates and (b) inner-coordinates. The solid lines denote the data from [?] at a similar $Re$ . . . . .	26
5.3	Wall-normal profiles of mean temperature plotted in (a) outer-coordinates and (b) inner-coordinates. Shading denotes a $\pm 5\%$ variance in computed $u_\tau$ value. The dotted line denote the data from Arya <i>et al.</i> [?] at $Re_\theta = 2290$ . . . . .	28
5.4	(a) Representative ensemble-averaged IR image of temperature step. The top-plate is unheated where $T=25^\circ\text{C}$ and the bottom plate is set to $T=40^\circ\text{C}$ . The flow is from top-to-bottom. (b) The streamwise profile of spanwise averaged temperature. . . . .	28
5.5	Wall-normal profiles of mean temperature after thermal step. Plates heated corresponding to profiles is as follows; #9 , #8-9 , #7-9 , #6-9 , #5-9 , #4-9 , #3-9 , #2-9 , #1-9 . Plotted in (a) inner-coordinates using $St$ (Eq. 2.2), and (b) modified inner-coordinates using $St_T$ (Eq. 5.2), subsequent profiles are offset by $\Theta^+ = 6$ for visual clarity. The dotted line denotes the law of the wall turbulent profile. . . . .	30
5.6	Spatial temperature distributions located downstream of a hemisphere for four values of $Re_D$ . The streamwise and spanwise positions have been normalized by the hemisphere diameter $D = 3\text{cm}$ . . . . .	31
5.7	Two plane view of cartoon depiction for resulting flow field from hemisphere perturbation. The XZ plane provides a birds eye view of the developing vortex wake, and the YZ plane provides a view of vortex wake downstream of the hemisphere and the resulting wall temperature. . . . .	33
5.8	Spanwise temperature profiles taken from the center of the IR images at a downstream position of 1 controller, ; 2 controllers, ; 3 controllers,  . . . . .	34
B.1	(a) insulation (b) frame. . . . .	38
B.2	(a) insulation (b) frame. . . . .	38
B.3	(a) insulation (b) frame. . . . .	39

B.4	(a) insulation (b) frame.	39
B.5	(a) insulation (b) frame.	40
B.6	(a) insulation (b) frame.	40
B.7	part	40

## **ABSTRACT**

### **Experimental Investigations into Thermal Pulsatile Boundary Layer flow**

by

Drummond Biles

University of New Hampshire, May, 2019

The need to reliably analyze, predict, and control the transport of mass, momentum, and energy in turbulent boundary layers is critically important across a broad spectrum of technological applications and scientific disciplines. While there has been extensive—and—continuing research investigating laboratory-scale canonical wall-bounded flows, beyond the scope of these well-studied flows there exists a broad range of application relevant flows that are far less studied. The theme of my dissertation research is to study such flows. The specific objective is to advance the knowledge based of boundary layer dynamics at high Reynolds number and in non-equilibrium. The strategy employed to achieve this objective is to perform detailed experimental measurements in purpose built facilities. The experimental measurement data will be analyzed within a first-principles framework to better understand the underlying flow physics of boundary dynamics at high Reynolds number and when influenced by non-equilibrium effects.

# **CHAPTER 1**

## **INTRODUCTION**

Boundary layers form when a fluid flows tangentially to a no-slip surface boundary (e.g. a solid wall) [?]. If a temperature difference exists between the no-slip surface boundary and the fluid, a thermal boundary layer will form as well [?]. By definition, boundary layers are very thin compared to a characteristic geometric dimension of the no-slip surface (e.g., the length of a solid wall over which the fluid flows). In spite of its relative thinness, the dynamics internal to the boundary layer determine the rate at which mass, momentum, and energy are transferred between the fluid and the surface boundary. In the majority of engineering systems as well as geophysical flows, the dynamical flow state of the boundary layer is turbulent. It follows that the need to reliably analyze, predict, and control the transport of mass, momentum, and energy in turbulent boundary layers is critically important across a broad spectrum of technological applications and scientific disciplines [?]. Owing to this importance, there has been extensive—and continuing—research to better understand the underlying boundary layer transport mechanisms at work [?]. The extensive body of research includes experimental, theoretical, and numerical studies, where the overwhelming majority of these studies have focused on laboratory-scale canonical wall-bounded flows such as fully-developed pipe and channel flow or zero pressure gradient (ZPG) boundary layer flow. It is fair to say that much has been learned about the dynamics of these canonical flows [?], although there is much still to learn [?, ?]. Significantly less, however, is known about flows that fall outside the domain of these well-studied flows.

The broad objective of this dissertation is to better understand (a) the boundary layer structure at high Reynolds numbers and (b) heat transfer in non-equilibrium boundary layers. Although the experimental investigations of (a) and (b) can be considered independent as they are conducted in different flow facilities and with different initial and boundary conditions, the unifying theme

of the dissertation is to expand the knowledge base of turbulent boundary layer dynamics beyond canonical laboratory-scale flows. Moreover, it is important to study the types of flow investigated in this dissertation for practical purposes since many natural and engineering fluid flows are at high Reynolds number (e.g., atmospheric flows and flow around large-scale aviation and marine vessels). Similarly, heat transfer in non-equilibrium wall bounded flow plays a critical role in the performance, efficiency, and life-cycle of many engineered systems (e.g., piston engine, gas turbines).

## **Boundary Layers**

### **Thermal Boundary Layers**

### **Non-Equilibrium Boundary Layers**

### **Experimental Investigations**

A momentum boundary layer forms when a fluid flows through or over a body that has a no-slip surface boundary (e.g. a solid wall) [?]. If a temperature difference exists between the no-slip surface boundary and the fluid, a thermal boundary layer will form as well [?]. The size of the thermal boundary layer relative to the momentum boundary layer will depend on the Prandtl number,  $Pr = \nu/\alpha$ , where  $\nu$  and  $\alpha$  are the kinematic viscosity and thermal diffusivity of the fluid, respectively. In spite of its relative thinness compared to the size of the body, the dynamics of the boundary layer determine the rate at which mass, momentum, and energy are transferred between the fluid and the surface boundary. In the majority of engineering systems as well as geophysical flows, the dynamical flow state of the boundary layer is turbulent. It follows that the need to reliably analyze, predict, and control the transport of mass, momentum, and energy in turbulent boundary layers is critically important across a broad spectrum of technological applications and scientific disciplines [?]. Owing to this importance, there has been extensive and continuing experimental, theoretical and numerical research to better understand the underlying transport

mechanisms at work [?]. The extensive body of research includes experimental, theoretical, and numerical studies, where the overwhelming majority of these studies have focused on so-called canonical wall-bounded flows such as fully-developed pipe and channel flow or ZPG boundary layer flow. It is fair to say that much has been learned about the dynamics of these canonical flows [?], although there is much still to learn [?, ?]. Significantly less, however, is known about the dynamics of non-equilibrium boundary layer flows. The need to address this knowledge gap is important since many application relevant and geophysical flows exhibit non-equilibrium boundary layer behaviors [?].

In canonical equilibrium boundary layer flows, the time scales over which the mean field vary are large compared to local turbulent time scales. The turbulent field rapidly adjusts to mean field variations, and the flow exhibits universal behaviors when scaled by local parameters [?]. One very important universal behavior is the logarithmic dependence of the mean velocity profile  $\bar{u}$  in the so-called logarithmic region,

$$\bar{u}^+ = \frac{1}{\kappa} \log(y^+) + C_1, \quad (1.1)$$

where the superscript  $^+$  denotes normalization by the friction velocity  $u_\tau = \sqrt{\tau_w/\rho}$  and kinematic viscosity  $\nu$ , where  $\tau_w$  is the shear stress at the wall and  $\rho$  the fluid density;  $1/\kappa$  (typically  $\kappa$  is called the von Kármán coefficient) is the slope;  $y^+$  is the wall-normal coordinate; and  $C_1$  is the intercept at  $y^+ = 1$ . Equation 2.3 is referred to as the law of the wall with coefficients (at sufficiently high Reynolds number)  $\kappa \approx 0.4$  and  $C_1 \approx 5$ , varying for a given canonical flow type [?].

The temperature distribution in the boundary layer, using similar dimensional scaling arguments used to derive Eq. 2.3, yields the law of the wall for the mean temperature distribution,

$$\overline{\Theta^+} = \frac{\overline{T_w - T(y)}}{\overline{T_\tau}} = \frac{1}{\kappa_T} \log(y^+) + C_2(Pr), \quad (1.2)$$

where  $T_w$  is the wall temperature,  $T(y)$  is the temperature in the boundary layer, the superscript  $^+$  denotes normalization by the friction temperature  $T_\tau = q''_w/(\rho c_p u_\tau)$ , where  $q''_w$  is wall heat flux,  $c_p$

is specific heat and  $u_\tau$  is the friction velocity. The dimensionless coefficients  $1/\kappa_T$  is the slope and  $C_2$ , which is a function of  $Pr$ , is the intercept at  $y^+ = 1$ . In general at sufficiently high Reynolds number,  $\kappa_T \approx 0.48$  but also varies for a given canonical flow type [?].

In non-equilibrium boundary layers, the time scales over which the mean field vary are comparable (or smaller) to local turbulent time scales, and the flow field cannot be characterized solely in terms of local parameters [?]. Such rapid changes in the mean momentum field typically result from pressure gradients, wall curvature, strong three-dimensionality, wall roughness, or dynamic walls. For non-equilibrium boundary layers in which an equilibrium boundary layer flow experiences a localized perturbation (e.g., flow over an obstacle/cavity or flow subjected to a pressure gradient), there has been considerable, and continuing, research to understand the redistribution of the momentum field when the equilibrium state is disturbed [?, ?, ?, ?]. In general, these studies show that: (a) in a small local region near the perturbation the log-layer is obliterated (i.e., the law of the wall given by Eq. 2.3 does not hold), (b) downstream of the perturbation, in the so-called recovery region, an internal stress equilibrium layer grows and the boundary layer recovers towards equilibrium. Conceptually, the effect of (b) relative to Eq. 2.3 is a spatially developing slope and intercept that approach their universal values at the edge of the recovery region; the functional form of the spatial dependence depending on the perturbation.

While the effects of non-equilibrium boundary layers on the velocity field have been considerably studied, heat transfer in non-equilibrium boundary layers has received far less attention. Nevertheless, despite somewhat limited data, it is a well-accepted fact that the law of the wall for temperature is more affected by mean field variations than the velocity field [?, ?, ?, ?, ?, ?]. For example, in non-equilibrium boundary layer flow subjected to a pressure gradient, the constants in Eq. 2.4 vary significantly with pressure gradient while the constants in Eq. 2.3 vary little. This difference in sensitivity is unexpected given that Eqs. 2.3-2.4 were derived from analogous dimensional scaling arguments, and has brought into question the validity of the law of the wall [?]. Moreover, the high sensitivity of the temperature field to pressure gradient flows is remarkable since the pressure gradient does not appear in the transport equation for temperature. The consen-

sus, although not entirely well-understood, is that while the law of the wall for velocity is fairly resilient, the law of the wall for temperature is very strongly affected by upstream disturbances. The implication is that the scaling used to derive the law of the wall fails to describe the behaviors of the mean dynamics (especially for temperature) when there are large gradients in the mean flow direction. Consequently, to capture non-equilibrium effects on mean field dynamics, the present state of the research is to reformulate the law of the wall through the use of new scaling laws [?, ?, ?, ?, ?] or use single-point closure models (i.e., eddy viscosity or mixing length models) informed by experimental or numerical data [?].

Extrapolating the results discussed above to *strong* non-equilibrium flows, in which mean field perturbations vary rapidly in magnitude both spatially and temporally (e.g., in-cylinder engine flows or other reciprocating machinery), a logical conclusion with respect to the law of the wall is that Eqs. 2.3-2.4 will either (a) not hold or (b) the slope and intercept will vary strongly in space and time. Moreover, the high sensitivity of the temperature field to mean field perturbations strongly suggests that computational fluid dynamic (CFD) simulations utilizing wall functions based on equilibrium boundary layer behaviors will not accurately capture heat transfer in strong non-equilibrium flows or perhaps even fail spectacularly [?].

The potential for CFD simulations to accurately predict boundary layer transport depends on the specifics of the closure model and wall functions used. In general, the development of turbulent closure models and wall functions are informed, refined, and validated by experimental data. One obstacle for formulating new engineering heat transfer models that better captures the physics of non-equilibrium flows (i.e., flows with complex dynamics) is the lack of robust experimental data needed to both develop and validate models.

The lack of experimental studies is not surprising given that controlling thermal boundary conditions is non-trivial, and the simultaneous measurement of temperature and velocity fluctuations in turbulent boundary layers with heat transfer is very difficult. In addition, direct measurement of the wall-heat flux, which is the primary scaling variable to study thermal boundary layers, is challenging. The aim of the present work is to develop a unique thermal wall plate that can be

used to control the thermal boundary conditions in non-equilibrium boundary layer flows. Owing to the strong spatial variations of the flow associated with non-equilibrium boundary layers, this is a nontrivial but important objective needed to better understand thermal transport in these types of flows. The facility described here, the Non-Equilibrium And Thermal (NEAT) boundary layer wind tunnel, will be used to advance the fundamental knowledge base of non-equilibrium boundary layer transport as well as to develop and validate Reynolds-Averaged-Naiver Stokes (RANS) turbulence models for non-equilibrium thermal boundary layer flows. For the latter use, the ability to modify the thermal conditions in a variety of ways is beneficial so that RANS models can be tested and validated in uniquely different flows but in the same flow facility using the same measurement techniques. The need for the facility and corresponding measurements is evident by the fact that the experimental measurement of Perry *et al.*[?] and Blackwell *et al.*[?] remain the primary datasets utilized in the validation of DNS of thermal boundary layers [?]

## CHAPTER 2

## THEORY

### Boundary Layers

-detail general equations for boundary layer flow and describe assumptions made to arrive at equations and empirical formulations based off of equation. Boundary layer thickness,

### Reynolds Analogy

-Detail how BL work is imposed onto the velocity field and show the similarities between the two field transport equations. Discuss Reynolds analogy,

Here

$$\Theta = \frac{T_w - T(y)}{T_w - T_\infty}, \quad (2.1)$$

where  $T_\infty$  denotes the freestream temperature. The inner normalization is described in Eq. 2.4. The value of the wall heat flux needed for the inner-normalization was approximated using Colburns formulation given by

$$St_T = \frac{q''_w}{\rho c_p U_\infty (T_w - T_\infty)} = Pr^{-2/3} \left( \frac{u_\tau}{U_\infty} \right)^2 \quad (2.2)$$

where

## Non-equilibrium Flow

-Discuss how momentum fields depart from equil when non-equil behavior is introduced. Discuss thermal field, break down of Reynolds analogy

## Determination of Wall Heat Flux

In canonical equilibrium turbulent boundary layer flow, the time scales over which the mean field vary are large compared to local turbulent time scales. The turbulent field rapidly adjusts to mean field variations, and the flow exhibits universal behaviors when scaled by local parameters [?]. One very important universal behavior is the logarithmic dependence of the mean velocity profile in the so-called logarithmic region,

$$\bar{u}^+ = \frac{1}{\kappa} \log(y^+) + C_1, \quad (2.3)$$

where an overline denotes a mean quantity, the superscript  $+$  denotes normalization by the friction velocity  $u_\tau = \sqrt{\tau_w/\rho}$  and kinematic viscosity  $\nu$ , where  $\tau_w$  is the shear stress at the wall and  $\rho$  the fluid density;  $1/\kappa$  (typically  $\kappa$  is called the von Kármán coefficient) is the slope;  $y^+$  is the wall-normal coordinate; and  $C_1$  is the intercept at  $y^+ = 1$ . Equation 2.3 is referred to as the logarithmic law of the wall with constants (at sufficiently high Reynolds number)  $\kappa \approx 0.4$  and  $C_1 \approx 5$ , varying for a given canonical flow type [?]. For the distribution of temperature in the boundary layer, using similar dimensional scaling arguments used to derive Eq. 2.3, yields the law of the wall for the mean temperature distribution,

$$\bar{\theta}^+ = \frac{\overline{T_w - T(y)}}{T_\tau} = \frac{1}{\kappa_T} \log(y^+) + C_2(Pr), \quad (2.4)$$

where  $T_w$  is the wall temperature,  $T(y)$  is the temperature in the boundary layer, the superscript  $+$  denotes normalization by the friction temperature  $T_\tau = q''_w / (\rho c_p u_\tau)$ , where  $q''_w$  is wall heat flux, and  $c_p$  is specific heat. The dimensionless coefficients  $1/\kappa_T$  is the slope and  $C_2$ , which is a function

of Prandtl number  $Pr$ , is the intercept at  $y^+ = 1$ . In general,  $\kappa_T \approx 0.48$  is taken as a universal constant.

In non-equilibrium boundary layers, the time scales over which the mean field vary are comparable (or smaller) compared to local turbulent time scales, and the flow field cannot be characterized solely in terms of local parameters [?]. Such rapid changes in the mean momentum field typically result from pressure gradients, wall curvature, strong three-dimensionality, wall roughness, or dynamic walls. A major focus of non-equilibrium boundary layer flow research is to understand the redistribution of the velocity field when equilibrium is disturbed [?, ?, ?, ?]. In general, these studies show that: (a) in a small local region of a strong perturbation the log-layer is obliterated (i.e., the law of the wall given by Eq. 2.3 does not hold), (b) downstream of the perturbation, in the so-called recovery region, an internal stress equilibrium layer grows and the boundary layer recovers towards equilibrium. Conceptually, the effect of (b) relative to Eq. 2.3 is a spatially developing slope and intercept that approach their universal values at the edge of the recovery region; the functional form of the spatial dependence depending on the perturbation.

While the effects of non-equilibrium on the velocity field have been reasonable well-studied, heat transfer in non-equilibrium boundary layers has received far less attention. *Nevertheless, despite somewhat limited data, it is a well-accepted fact that the law of the wall for temperature is more affected by mean field variations than the velocity field [?, ?, ?, ?, ?, ?].* For example, in non-equilibrium boundary layer flow subjected to a pressure gradient, the constants in Eq. 2.4 vary significantly with pressure gradient while the constants in Eq. 2.3 vary little. This difference in sensitivity is unexpected given that Eqs. 2.3-2.4 were derived from analogous dimensional scaling arguments, and has brought into question the validity of the law of the wall [?]. Moreover, the high sensitivity of the temperature field to pressure gradient flows is remarkable since the pressure gradient does not appear in the transport equation for temperature. The consensus, although not entirely well-understood, is that while the law of the wall for velocity is fairly resilient, the law of the wall for temperature is very strongly affected by mean-field disturbances. The implication is that the scaling used to derive the law of the wall fails to describe the behaviors of the mean dynam-

ics (especially for temperature) when there are large gradients in the mean-field. Consequently, to capture non-equilibrium effects on mean field dynamics, the present state of the research is to reformulate the law of the wall through the use of new scaling laws [?, ?, ?, ?, ?] or use single-point closure models (i.e., eddy viscosity or mixing length models) informed by experimental or numerical data [?]

The aim of the present work is to study heat transfer in various non-equilibrium boundary layer flow to better understand the effects of non-equilibrium on the temperature distribution and wall heat flux. A major thrust of this work was to develop a unique flow facility to produce and study non-equilibrium and thermal boundary layers. The key design component is a thermal wall plate that can be used to control the thermal boundary conditions in non-equilibrium boundary layer flows. Owing to the strong spatial variations of the flow associated with non-equilibrium boundary layers, this is a nontrivial but important objective needed to better understand thermal transport in these flows. The facility will be used to advance the fundamental knowledge base of non-equilibrium boundary layer transport as well as to develop and validate Reynolds-Averaged-Naiver Stokes (RANS) turbulence models of thermal transport in these flows. *For the latter use, the ability to modify the thermal boundary conditions in a variety of ways is beneficial so that RANS models can be tested and validated in uniquely different flows but in the same flow facility using the same measurement techniques.* The need for the facility and corresponding measurements is evident by the fact that the experimental measurement of Perry *et al.*[?] and Blackwell *et al.*[?] from the late 1960s and early 1970s, respectively, remain the primary datasets utilized in the validation of DNS of thermal boundary layers [?].

## **CHAPTER 3**

### **EXPERIMENTAL METHODS**

#### **Velocity Measurements**

-describe and detail measurements

#### **Thermal Measurements**

-describe and detail measurements

-Methods section from validation paper

The temperature of the thermal wall plate and the spatial uniformity of temperature are evaluated using a FLIR SC645 IR camera and J-type thermocouples embedded 2.5mm beneath the top surface of each aluminum plate. The spectral range of the camera is 7.5-13  $\mu m$ . The camera resolution is 640 pixel  $\times$  480 pixel and the measurement uncertainty is  $\pm 2\%$  of the measured temperature. The measurement uncertainty of the J-type thermocouples is 0.01°C as determined from examining the standard deviation of long time series collected at fixed temperatures.

The wall-normal profile of temperature within the thermal boundary layer is performed using a sting-mounted type J fine-wire thermocouple with a probe diameter of 0.65mm attached to a Velmex BiSlide traverse with a step resolution of 5  $\mu m$ . A Titan Tool Supply Co. Titan Measuring A-1 Microscope-Telescope cathetometer, with an accuracy of  $\pm 64 \mu m$  was used to locate the thermocouple position relative to the surface of the thermal wall plate. PIV was used to acquire planar fields of velocity in the streamwise/wall-normal plane (i.e., xy-plane in the chosen experimental coordinate system). Light is provided by a Photonics DM-series dual cavity Nd:YLF laser

capable of 30mJ per pulse. A periscope and a  $90^\circ$  turning mirror is used to direct the laser light into the tunnel test section. Sheet forming optics (cylindrical and spherical lenses) placed prior to the turning mirror are used to form a laser sheet on the order 1mm thick. The laser light is scattered by atomized oil droplets of  $1\mu m$  nominal diameter introduced into the flow in the seeding manifold upstream of the test-section inlet. Images of the laser light scattered off the tracer particles perpendicular to the incident laser sheets are acquired using two 12-bit Photron FASTCAM SA4 CMOS cameras.

The CMOS array size of each camera is 1024 pixel  $\times$  1024 pixel. The two cameras are placed on opposite sides of the tunnel and image the same plane but with different field-of-views (FOV). This is done to achieve high spatial resolution in the near wall region while still imaging the entire boundary layer. Camera 1 has a FOV ranging from  $2\text{mm} < y < 26\text{mm}$  and camera 2 has a FOV ranging from  $5\text{mm} < y < 54\text{mm}$ , where  $y=0$  is the bottom wall.

The PIV images were acquired at  $3.6kHz$  with a spatial resolution of  $0.4\mu m$  per pixel and analyzed using LaVision PIV software, DaVis 8.0.6 and DaVis 8.3.1. Cross-correlation algorithms between two successive images are used to determine the particle displacement field and the time separation between the images is used to determine the velocity field from the displacement field.

## CHAPTER 4

### NEAT BOUNDARY LAYER WIND TUNNEL

#### Experimental Facility

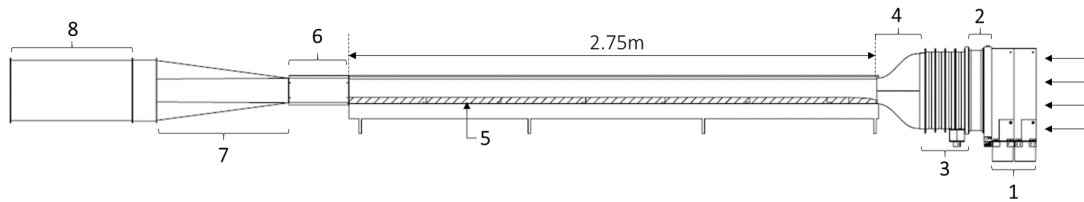


**Figure 4.1.** Schematic of the experimental facility. Air enters the facility from right-to-left. The primary components include: (1) freestream heaters, (2) seeding manifold, (3) turbulence management section, (4) contraction, (5) thermal wall-plate located on the bottom wall of the test-section, (6) rotor-stator assembly, (7) diffuser, (8) centrifugal fan.

The NEAT boundary layer wind tunnel is an open-circuit in-draft type designed to study heat transfer in non-equilibrium boundary layers. Figure 4.1 shows the design schematic for the facility. The key design component is the thermal wall plate used to control the lower-wall thermal boundary conditions seen by the flow.

#### General Description

The inlet section to the tunnel consists of a feed-back controlled resistive heater bank, a seeding manifold, a turbulent management section and a 4:1 contraction. The test-section of the tunnel nominally measures 303mm × 111mm cross-section and 2.75m in length and is made of plexiglass to allow optical access. Removable windows in the top wall of the tunnel sit at 45, 136.3, and 251.8 cm from the test section inlet which allow for the introduction of probes, laser light, or IR measurements into the tunnel test section. A feed-back controlled thermal wall-plate sits on the

floor of the test section and is used to control the lower-wall temperature seen by the flow. The leading edge of the thermal wall-plate is a super-ellipse designed to prevent flow separation [?]. The upper wall of the test-section is angled at  $0.23^\circ$  to closely maintain a ZPG condition along the length of the test-section. Downstream of the test-section is a pulsatile flow generator used to produce a sinusoidal pressure gradient, creating a non-equilibrium flow condition. The diffuser transitions the flow area from a rectangular to a circular cross-section where it connects to a belt driven centrifugal fan. A frequency controller is used to control and maintain the fan speed and corresponding flow speed in the test-section. The freestream velocity in the test-section can vary between 1 and  $12ms^{-1}$ . The entire tunnel sits on a custom frame which levels and isolates the tunnel test-section. In the following subsections, the components of the facility are described in detail.

## Inlet Section

Air entering the test-section first passes through an OMEGA Engineering air duct heater (model CABB-1211/208). The 3-phase 208V heater consists of nine sheathed finned chrome steel resistive heaters that provide 12 kW of power (with a power density of  $4.03\text{ W/cm}^2$ ). The cross-sectional area of the heater is  $390.5\text{mm} \times 358.8\text{mm}$  with an open area of  $859.4\text{ cm}^2$  (blockage of about 39%). The three legs of the AC power are connected to the heater through a Watlow Din-A-Mite C silicone controller rectifier (SCR) power controller. A type J thermocouple placed in the freestream 1m downstream of the test-section inlet provides feedback for a proportional, integral, and derivative (PID) controller used as the input for the SCR power controller. The SCR power controller, configured for zero-voltage crossover firing (as opposed to phase angle crossover firing) to reduce electrical noise, is used to regulate the duty cycle of the voltage (either 0% or 100%) to the heaters thereby controlling the freestream temperature. A SCR power controller was chosen (over a mechanical relay or solid state relay) as it is more suitable for handling the large current (33.4A) needed for the heater and has a fast response time of 5.56ms, which not only allows for

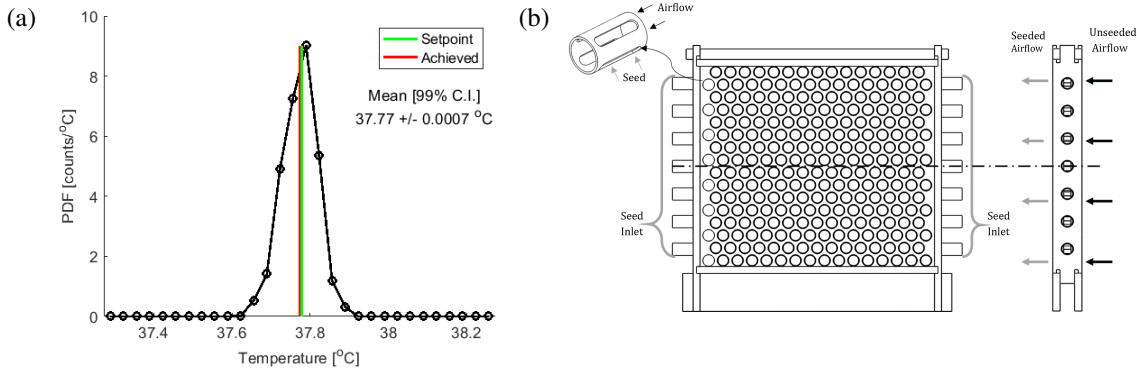


**Figure 4.2.** (a) Probability density function (PDF) of freestream temperature measured in the wind tunnel over a two hour period. The vertical green line represents the setpoint temperature and the vertical red line represents the measured mean temperature with a confidence interval of 99%. (b) Schematic of the seeding manifold used for particle image velocimetry (PIV).

a tightly controlled freestream temperature but also prolongs the life of the heating elements by reducing the thermal fatigue.

The PID controller gains are optimized for varying freestream velocity and temperature conditions, as one set of gain values does not work well over a large operating range. This is achieved using the autotune feature of the SCR power controller-PID feedback system. The ability of the system to hold a freestream set point temperature is shown in Fig. 4.2(a). After exiting the heater, the air flow passes through a honeycomb-type seeding manifold to introduce (if desired) tracer particles into the flow to be used for particle image velocimetry (PIV). The challenge with seeding an open-circuit wind tunnel is that the flow tracers must be uniformly distributed into the flow at the source. This is much more difficult than seeding a closed-circuit wind tunnel where the seed can be allowed to circulate through the facility to produce a uniform seed concentration.

The custom designed seeding manifold is shown in Fig. 4.2(b). The inlet air flows across the manifold through 248 PVC tubes of length 38.1mm and diameter 21.34mm. Four slots of 25.4mm length and 6.35mm width separated by 90° (center-to-center) are cut into each PVC tube. The plenum volume of the seeding manifold is filled with a dense fog of nominal 1 $\mu$ m diameter oil droplets [?] through up to twenty-three 21.34mm diameter pipes mounted around the perimeter of

the seeder connected to a ROSCO 1700 fogger. The fog is drawn into the PVC inlet air piping through the four slots owing to the pressure difference between the fog in the plenum and the air in the PVC tubes. The open area percentage of the manifold (56.5%) is comparable to the open area of the freestream heater (61%). Detailed drawings of the seeding manifold can be found in App. A. The air then passes through a turbulence management section containing 4 screens of decreasing wire mesh size and then a honeycomb section. The screens reduce axial turbulence while the honeycomb reduces lateral turbulence. The air flow then proceeds through a 4:1 contraction to speed up the flow and to further reduce turbulent intensities.

## Test Section

To investigate turbulent boundary layers, a 3mm diameter trip rod extending the spanwise extent of the test-section is placed on the rear of the leading-edge nose, just upstream of the first convective plate. The rod induces transition to turbulence and fixes (on average) the starting location of a developing turbulent boundary layer. A range of trip diameters as well as shape were tested to determine the smallest diameter which would lead to a steady (on average) transition. An undersized trip does not induce enough energy and the flow can relax back to a laminar state, while too large of a trip produces near wall effects which do not decay in an appropriate range [?]. Wall normal velocity profiles taken at the first measurement location verified the appropriate trip diameter by comparing mean profiles as the recovery length does not depend on the order of the statistic measured [?].

Three windows of size 254mm  $\times$  102mm sit in the top wall of the test-section located at approximately 45, 136.3, and 251.8cm from the test-section inlet. The windows are used for introduction of laser light, for infrared (IR) imaging and for inserting various measurement probes. The window body, seen in Fig. 4.3, contains 4 leveling screws such that window can be set flush with the inside wall of the tunnel. Window inserts made from either BK7 glass or clear polycarbonate can be installed depending on the requirement. The optical quality of the glass inserts are better than the plexiglass walls and necessary for IR imaging. The tunnel frame, which supports

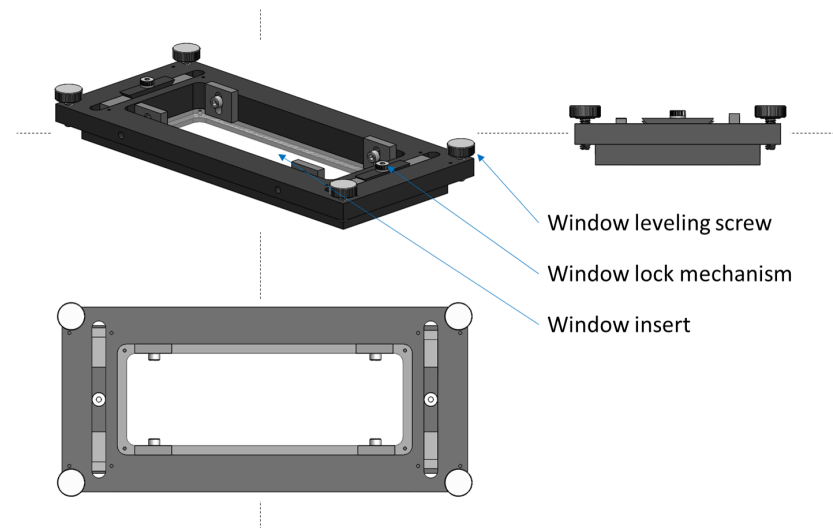


**Figure 4.3.** Schematic of removable windows which allow for optical measurements and installation of temperature/velocity probes. Design was developed by Dr. Michael Allard

the working section of the tunnel, has leveling adjustments in the x and z direction such that the tunnel floor sits parallel to the adjacent optics table. This then orients the x-y plane of the tunnel and any optical equipment mounted to the optical table. Custom optics mounting boards line the streamwise length of the tunnel for ease of experimental setup. The entire frame sits on damping feet which isolate the tunnel from any ambient vibrations in the room.

## Thermal Wall-plate

### Prototype Wall-plate

The thermal wall plate covers the bottom floor of the NEAT test section and controls the bottom wall boundary condition by setting  $T_{wall}$ . The design is modeled after the work of Blackwell et al. [?]. The base design consists of a thermal mass which is heated and maintained at a set temperature. The main design condition was that the system must be able to maintain a set wall temperature independent of the above flow state (i.e. 2-D varying wall heat flux). Other design constraints were to minimize the height of the system so as to reduce blockage effects; minimize conductive heat loss from the thermal mass so as to ensure all heat was going into convective

transfer; and to design a system which could be manufactured in house and installed with ease into the NEAT tunnel.

For prototype development a different open circuit down draft wind tunnel was used as it had a smaller development length and had a greater ease of access to the working section. The working section of the tunnel is  $0.45\text{m} \times 0.45\text{m} \times 0.66\text{m}$  ( $z$  by  $y$  by  $x$ ). To account for the streamwise variation in heat flux (coming from a developing boundary layer) the prototype design consisted of two thermal masses with increasing streamwise length based on downstream location. This also assisted in ease of manufacturing as the parts could then fit within the working area of the UNH machine shop.

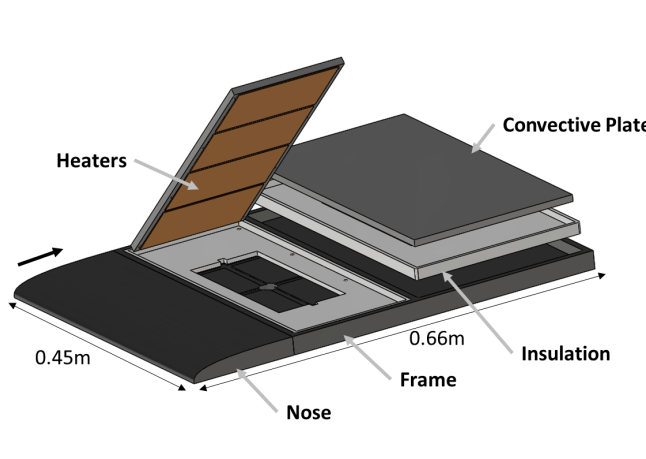


**Figure 4.4.** Solid model of prototype thermal wall plate with two convective plates.

Fig. 4.4 shows the solid model design of the prototype thermal wall plate. The thermal mass is an aluminum 6061 plate which is  $0.675"$  thick (CHECK THIS). For heating the Al plate, there is an array of Kapton polyimide-film resistive resistive heaters (affixed to the bottom of the aluminum plate) with a heating density of  $1.5\text{W/cm}^2$ . In between the heaters there are a series of holes which contain J-type thermocouples, which then sit  $2.5\text{mm}$  beneath the surface of the plate and act in a feed back loop to control the thermal mass temperature. Each Al plate sits into a custom machined section of insulation made from calcium-silicate. Each of the insulated wall plates then sit into

a frame manufactured from Delrin which sets the spacing of each plate, and was chosen for its low thermal conductivity and machinability. Due to the desire of producing high quality physics grade boundary layers a leading edge nose was developed to smoothly transition the flow onto the thermal wallplate. The nose utilizes a super-ellipse design to prevent flow separation [?] which was determined according to Eqn. 1 of Narasimha et al;

$$[(a - x)/a]^2 + (y/b)^2 = 1 \quad (4.1)$$

where x is the streamwise position, y is the wall normal position, a is the length of the nose, 2b is the height of the nose. To accurately recreate the desired profile a three-axis controlled CNC machine was used to smoothly cut the profile into the Delrin. Fig. 4.6 shows the fabrication process applied to the final implemented design.

The prototype design was used for testing and developing wall temperature control schemes. A variety of measurements were made with the plate including; ZPG wall temperature distribution, and wall temperature distribution due to wake behind a hemisphere. The ZPG conditions validated the base design and demonstrated that ZPG thermal boundary layer developed as expected when compared to literature. The wake study gave insight into the performance of the design in complex flow states. It was found that future designs should utilize spanwise oriented bottom heaters as streamwise oriented heaters require individual zone control, where multiple controllers would be used to control the temperature of a single plate. The final design for installation into the NEAT tunnel incorporates many lessons learned from the prototype plate such as from manufacturing limits, material limits, and ease of operation and repair.

### **Finalized Wall-plate**

The final thermal wall-plate (shown in Fig. 4.5) comprises of twelve sections each independently heated and controlled. Each section consists of a 9.5mm thick aluminum 6061 plate, Kapton polyimide-film resistive resistive heaters (affixed to the bottom of the aluminum plate) with a heating density of  $1.5\text{W/cm}^2$ , and a 5mm thick calcium silicate holder used for thermal isolation

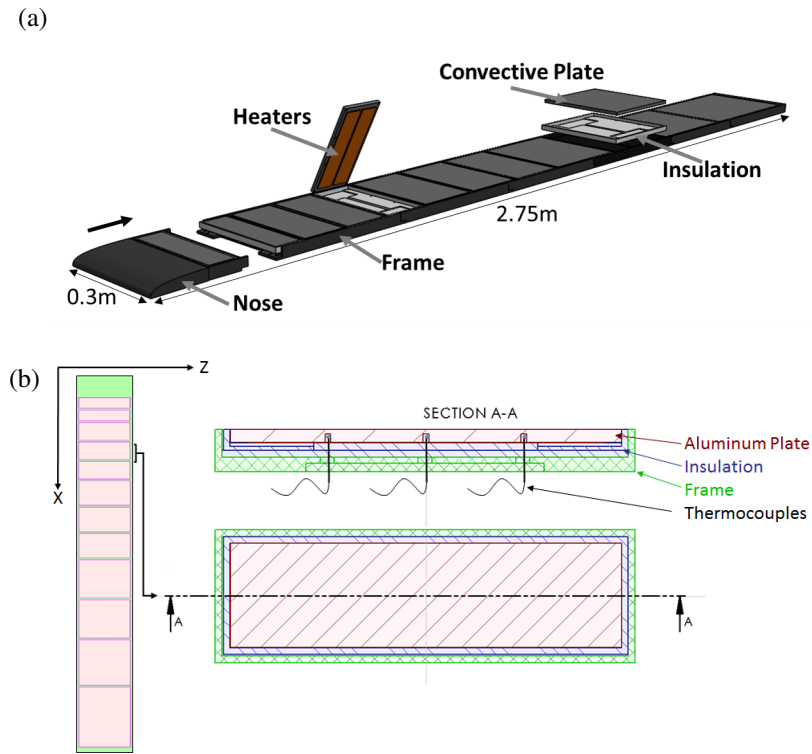


**Figure 4.5.** (a) Solid model schematic of the thermal wall-plate. (b) Detailed schematic of a section of the thermal wall-plate: right tilted  $45^\circ$  lines denotes the heated wall plate, left tilted  $45^\circ$  lines shows the surrounding layer of calcium silicate insulation and the hash marked section represents the co-polymer acetal frame which positions all components. Three evenly spaced embedded thermocouples are located along line AA.

of the aluminum plate (the thermal conductivity of the calcium silicate is four-orders of magnitude less than the aluminum 6061). Three evenly spaced J-type thermocouples arranged spanwise in the center of each plate and embedded 2.5mm beneath the top surface of each aluminum plate are used to monitor wall temperature for feedback control of wall heating. To increase ease of assembly and repair a thermocouple holder was designed to maintain the position of each thermocouple throughout assembly and operation. To ensure each thermocouple had adequate contact with the thermal mass each thermocouple hole was filled with a silver grease compound which is thermally conductive and electrically insulative. The section components sit in a Delrin (acetal) frame, which incorporates a method of leveling each section individually such that the overall surface roughness of the assembly can be reduced. The streamwise (flow direction) length of each section increases

**Table 4.1.** The length of the convective plates. Plate 1 is at the upstream end and plate 12 is at the downstream end of the wind tunnel.

Plate number	Length (mm)	Plate number	Length (mm)
1, 2	75	3, 4, 5	125
6, 7, 8	175	9, 10	275
11	325	12	425

with downstream position such that the convective heat transfer from plate-to-plate does not vary by more than a suitably chosen threshold of 15%. This threshold is set by examining the smallest feasibly manufacturable streamwise plate length of the most upstream plate, as this is where the heat flux changes most rapidly. The length of the plates are summarized in Table 4.1.

The entire wall plate system was design in a manor such that it could be assembled/disassembled with only one person. Interlocking frame sections are custom fit to within -.127 +0 mm of the tunnel width such that the system can be assembled plate by plate and slid into the tunnel from the inlet. Routed wires for heater power and thermocouple output are fed out of bottom windows which match the position of the top windows. Details about the individual wall-plate components are the assembly process are listed in App. B.

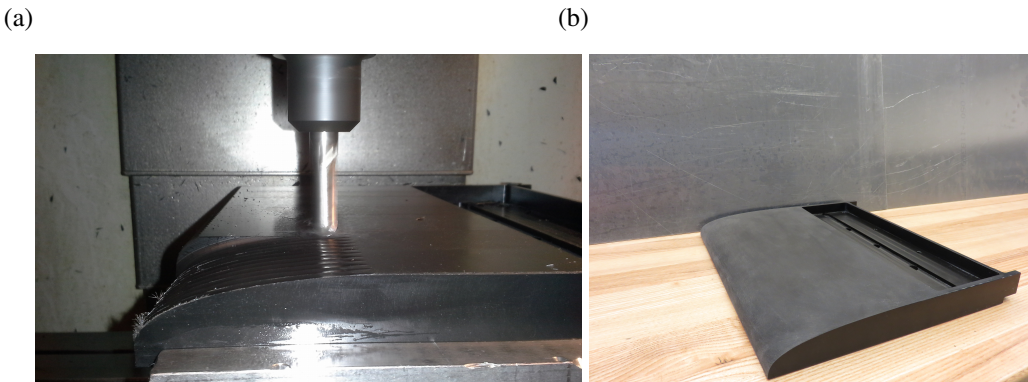


**Figure 4.6.** (a) Image of roughing pass for the fabrication of the super-ellipse leading edge nose of the wall plate (b) final image of leading edge frame component for the wall plate

The temperature of each section of the thermal wall-plate is monitored and maintained by its own feedback controller as illustrated in Fig. 4.7. LabVIEW is used to define and implement the

controller settings. Each controller consists of a 10A SCR and an NPN transistor. The average temperature of the three embedded thermocouples in each convective plate serves as the feedback parameter to direct the SCR to block/pass the 110 VAC that powers the resistive heaters (effectively the SCR serves as a switch to quickly turn the heaters on/off). The time constant of the controller is significantly smaller than the time constant of any given convective plate so the controller can monitor and adjust the heat-input to the convective plate much faster than the plate can lose (gain) heat to (from) the flow. The operating plate temperature range is 20°C to 65°C which is set by the working temperature of the materials used. The controller is able to set and maintain a temperature to within 0.5°C as determined from the variance of the embedded thermocouples during testing. Importantly, since the temperature of each section of the thermal wall plate is independently controlled, the design allows for the application of a wide-range of thermal boundary conditions: e.g., isothermal, streamwise temperature gradient, discrete temperature steps, among others.

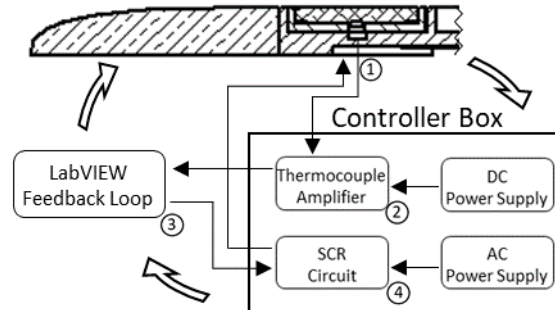


**Figure 4.7.** A diagram detailing the wall plate heater controller circuit. (1) designates the embedded thermocouples, which are fed to an amplifier (3), whose signal is then fed to a LabVIEW program (2), which determines if the heaters should be in an off or on position and sends a final signal to an SCR circuit (4), which communicates to the thermal wallplate heaters.

## Pulsatile Flow Generator

### Rotor-Stator Assembly

A rotor-stator assembly located downstream of the test-section was the first design used to generate a periodic pressure gradient used to produce a pulsatile freestream velocity in the tunnel.

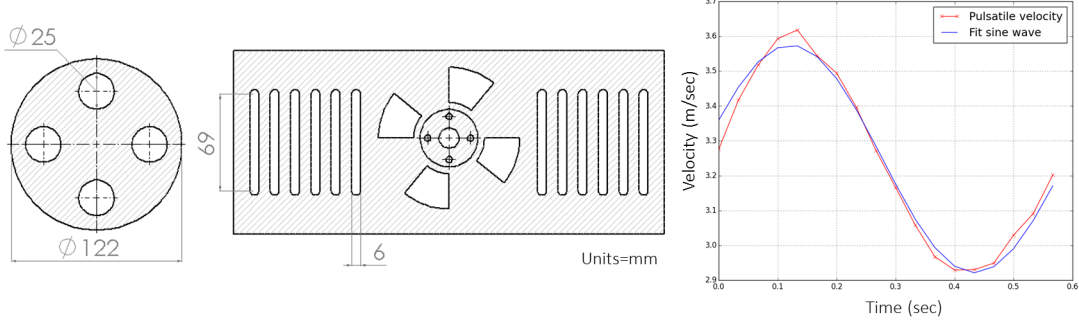


**Figure 4.8.** Schematic of rotor-stator design, left shows the rotor, shown in the middle is the stator, and the right plot depicts a freestream velocity time series taken with a pitot-static tube for a quarter revolution of the rotor-stator mechanism.

Pulsatile flows are periodic and unidirectional characterized by both their frequency and amplitude. The flow over a half-period first accelerates to maximum velocity then decelerates to the mean velocity. During the next half-period, the flow first decelerates to minimum velocity then accelerates to the mean velocity. In a pulsatile boundary layer flow, the acceleration/deceleration of the freestream velocity produces non-equilibrium flow behaviors. In particular, when the oscillation period is comparable to (or smaller than) the turbulence relaxation time (order  $100\nu/u_\tau^2$ , [?]), there will be a phase difference between the oscillating strain and stress field [?].

The design of the rotor-stator shown in Fig. 4.9. is modeled after the design of K.Al-Asmi *et al.* [?]. It consists of a rotor with 4 uniformly spaced holes, and a stator with 4 matching slots. The open area to the incoming flow is continuously modulated which produces a smooth sinusoidal freestream velocity signal as shown in Fig. 4.9(c). The rotor frequency is controlled via a DC motor with variable speed settings from 1-100Hz. Twelve air-bleed slots arranged on the stator control the ratio of fluctuating area to open area. The slots ensure the existence of a mean flow and by changing the ratio of fluctuating area to mean through area the pulsatile flow amplitude can be adjusted. In the present design, this area ratio can be adjusted from 40% to 100%. The rotor-stator assembly was mounted downstream of the test section to reduce the effect of induced rotational flow within the test-section. The assembly can be easily removed if a pulsatile flow is not desired.

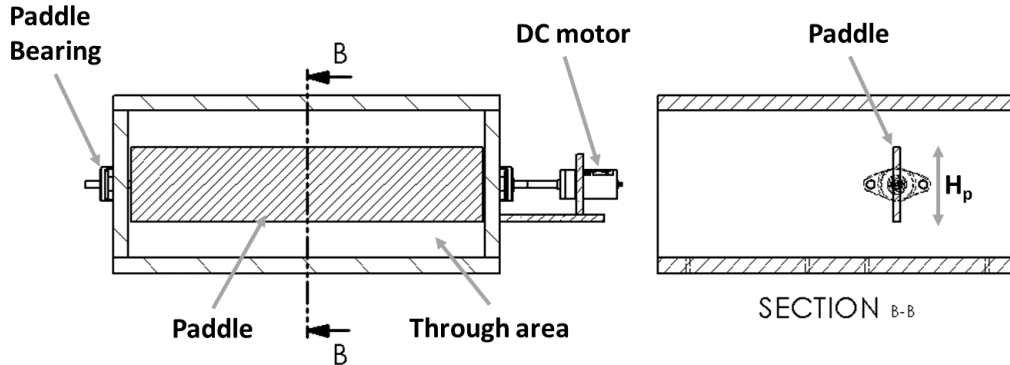


**Figure 4.9.** Schematic of pulsatile wave generator with a paddle design. The left image displays the y-z plane with flow going into the board, where the right figure shows a cutaway image with paddle height  $H_p$ .  $H_p$  can be adjusted for desired flow condition.

### Pulsatile Flow Generator

The rotor-stator mechanism went through a re-design process due to the desire for a design with a lower blockage ratio which would then allow for testing of higher  $Re$  flows. In XX et al. a vertical array of spanwise orientated paddles were rotated to create a pulsatile pressure wave. These paddles would create a similar sinusoidal change in through area yet drastically reduce the blockage ratio. A similar design was developed to fit within the rotor-stator mechanism box which uses 1 paddle that mounts into bearings on each spanwise wall. The paddle spans the entire width of the tunnel and connects to a DC gear motor **list exact motor** that sits outside the tunnel and operates in a feedback loop with an Arduino. Multiple paddles of varying heights can be installed to vary the fluctuating area. The blockage ratio is now reduced to 5% and  $Re$  up to XX can be reached.

## CHAPTER 5

### RESULTS AND DISCUSSION

#### Validation Tests

The thermal wall plate is validated for three test cases: nominal ZPG turbulent boundary layer flow (1) over an isothermal wall plate, (2) encountering a sharp step in wall temperature, and (3) around a wall mounted hemisphere body. Wall-normal profiles of temperature and velocity across the boundary layer are acquired for case (1) and (2). For case (3), IR imaging is used to show that the wall plate can maintain a constant temperature even when the flow above the wall is unsteady and strongly three-dimensional.

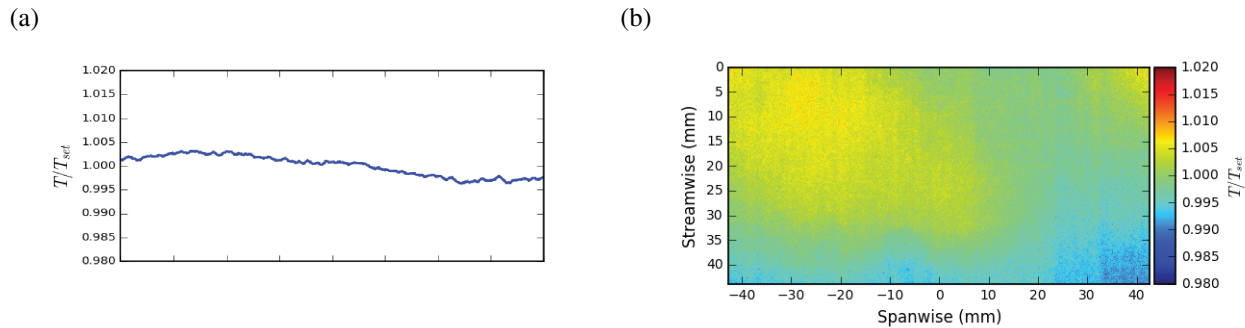


**Figure 5.1.** (a) Representative ensemble-averaged IR image of plate #5 for  $T_{set} = 40^\circ\text{C}$ . (b) Spanwise profile of streamwise averaged temperature from figure (a).

#### ZPG turbulent boundary layer flow over an isothermal wall plate

The freestream temperature of the air in the tunnel is set to  $25^\circ\text{C}$  and each section of the thermal wall plate is set to  $40^\circ\text{C}$ . Measurements are acquired at five different momentum thickness Reynolds numbers,  $Re_\theta$ , as listed in Table 5.1. The freestream velocity is steady with magnitudes

varying between 2–10 ms<sup>−1</sup>. The FLIR SC645 IR camera is positioned above plate #5 located 0.8m downstream of the trip and the FOV is 85mm × 64mm in the spanwise and streamwise directions, respectively. The temperature of the convective plate was evaluated by ensemble-averaging 100 IR images acquired at 16Hz to reduce pixel-noise. The effect of averaging over shorter or longer periods showed no statistical difference between the results.

Fig. 5.1(a) shows a representative ensembled-averaged IR image of the thermal wall plate. The colorbar represents  $T/T_{set}$  where  $T_{set}$  is 40°C. The range of the color bar magnitude is  $\pm 5\%$  of the set-point temperature. Spatially averaging the corresponding image in the streamwise direction results in the averaged spanwise temperature profile shown in Fig. 5.1(b). Note that the spanwise variation is less than the measurement uncertainty of the IR temperature measurement which is  $\pm 2\% \approx \pm 0.8^\circ\text{C}$ . In brief, the IR images show that the thermal wall plate can be held to a constant temperature within a tolerance that is less than the measurement uncertainty of the camera. The embedded thermocouples, located just downstream of Fig. 5.1(a) and at spanwise locations of 0 and  $\pm 75\text{mm}$ , indicate the spanwise gradient to be much smaller and that the tolerance of the wall plate temperature is  $\pm 0.5^\circ\text{C}$ .

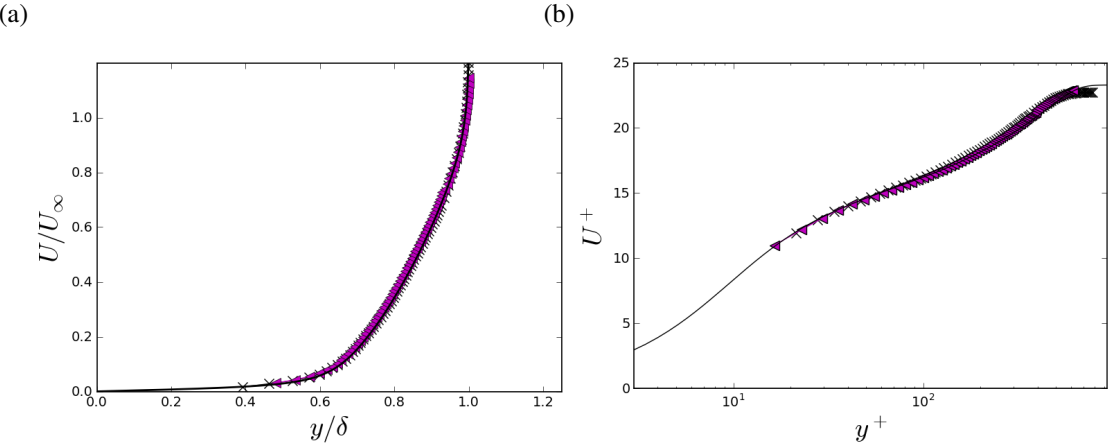


**Figure 5.2.** Wall-normal profiles of mean streamwise velocity at  $Re_\theta = 1527$  with thermal wall plate on ( $\times$ ) and off ( $\triangleleft$ ) plotted in (a) outer-coordinates and (b) inner-coordinates. The solid lines denote the data from [?] at a similar  $Re$ .

It is first shown that the momentum boundary layer behaves as expected, through the agreement with the DNS data, and the collapse of the two mean velocity profiles demonstrates that temperature behaves like a passive scalar. The wall-normal mean velocity profile was obtained by ensemble-averaging over 30,000 instantaneous PIV vector fields and then spatially averaging over the streamwise ( $x$ -) direction. The corresponding mean velocity profiles from camera 1 and camera 2 were then stitched together following the method of Shea *et al.* [?] to obtain a profile that spans the entire wall-normal height of the boundary layer. The outer normalized mean velocity profiles when the thermal plate was at 40°C and when the thermal plate was unheated is shown in Fig. 5.2(a) (all other conditions being the same), where  $U_\infty$  and  $\delta$  are the freestream velocity and momentum boundary layer thickness, respectively. The same profiles plotted in so-called inner coordinates are shown in Fig. 5.2(b) (see Eq. 2.3). Here the wall shear stress was computed from the PIV data using the integral method of Mehdi *et. al* [?]. The agreement with the DNS data and the apparent logarithmic region of the velocity profile demonstrates the flow over the plate is consistent with a canonical ZPG boundary layer.

**Table 5.1.** Parameters for measured temperature profiles

Symbol	$T_w$ (°C)	$U_\infty$ (ms <sup>-1</sup> )	$Re_\theta$	$\delta_T$ (mm)	$u_\tau$ (ms <sup>-1</sup> )
■	40	1.95	568	38	0.10
✗	40	2.87	825	34	0.14
◆	40	3.90	1147	34	0.17
◀	40	5.04	1454	33	0.22
●	40	9.15	2415	29	0.37

The wall-normal mean temperature profile was obtained by time averaging the thermocouple signal at a given  $y$ -position over a 100 seconds record length. Fig. 5.3(a) and Fig. 5.3(b) show the mean temperature profiles plotted in outer and inner-coordinates, respectively at five different values of  $Re_\theta$  as described in Table 5.1 .

Collectively, the two plots demonstrate that the measured temperature profile is consistent with a ZPG boundary layer over an isothermal wall with heat transfer.

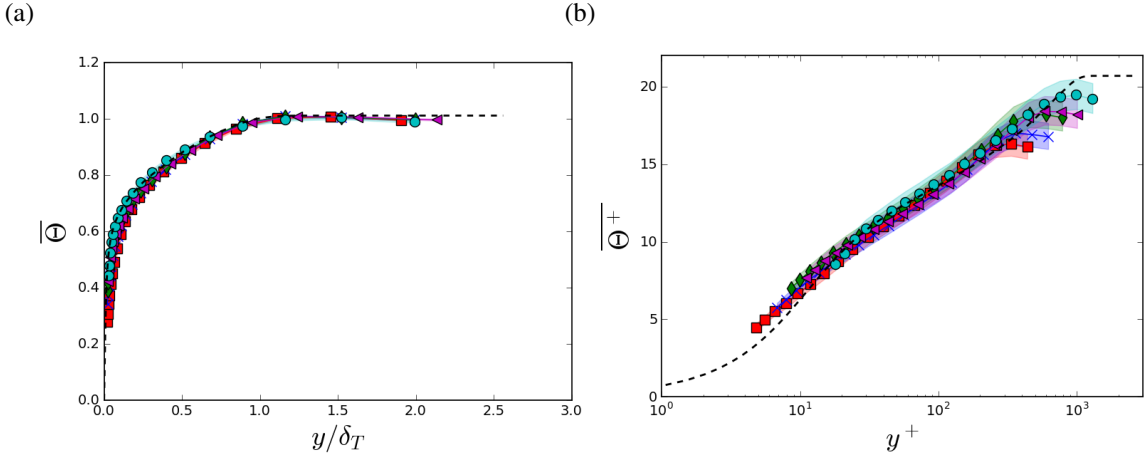


**Figure 5.3.** Wall-normal profiles of mean temperature plotted in (a) outer-coordinates and (b) inner-coordinates. Shading denotes a  $\pm 5\%$  variance in computed  $u_\tau$  value. The dotted line denote the data from Arya *et al.* [?] at  $Re_\theta = 2290$ .

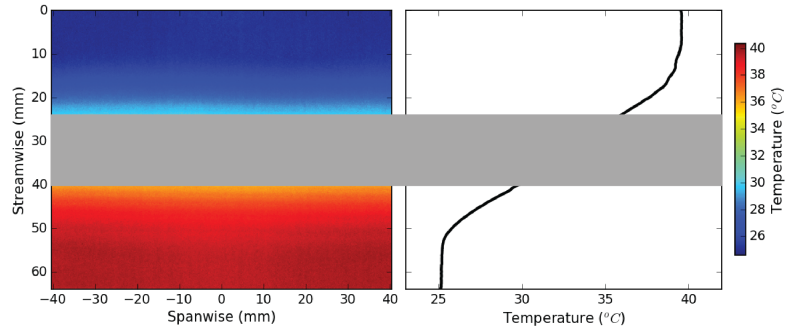


**Figure 5.4.** (a) Representative ensemble-averaged IR image of temperature step. The top-plate is unheated where  $T=25^\circ\text{C}$  and the bottom plate is set to  $T=40^\circ\text{C}$ . The flow is from top-to-bottom. (b) The streamwise profile of spanwise averaged temperature.

### ZPG boundary layer encountering a sharp step in wall temperature

In this configuration, a ZPG turbulent boundary layer initially develops over an unheated portion of the wall-plate and then encounters a sharp one-dimensional step in wall temperature at some distance  $x_T$  downstream of the boundary layer trip. Effectively, a thermal boundary develops internal to an existing turbulent momentum boundary layer. The configuration is relevant to a flow where a boundary layer encounters a change in surface conditions such as when the atmospheric

boundary layer flows from sea to land or when the flow over an engineered surface flows from a cold region to a hot region. Owing to its importance in both geophysical flows and engineering systems, this particular flow configuration has been fairly well-studied in the literature [?, ?, ?] and is therefore an appropriate test case for validating the NEAT boundary layer facility.

In the present study, the length of the unheated portion of the wall plate is varied by systematically changing the start location of the temperature step relative to the trip position. A sting-mounted type J fine-wire ( $0.65\text{mm}$  probe diameter) thermocouple attached to a Velmex BiSlide traverse was placed  $1.26\text{m}$  downstream of the trip (i.e., in the middle of plate #9). The freestream velocity was set to  $4\text{ms}^{-1}$  and wall-normal temperature profiles were acquired for varying unheated starting lengths. The temperature of the convective plate where the temperature step occurred and those downstream of the step were set to  $40^\circ\text{C}$  while the convective plates upstream of the step were unheated. In terms of the convective plate numbers, the first profile was acquired when only plate #9 was heated, the second profile was acquired when plates #8 and #9 were heated and so forth until the last profile was acquired when plates #1-9 were heated. Note that in this configuration, the thickness of the momentum boundary layer within which the thermal boundary layer begins to grow varies from profile to profile.

Fig. 5.4(a) shows a representative ensembled-averaged IR image of the temperature step. The flow is from top-to-bottom and the colorbar represents the surface temperature of the plate. The top-plate is unheated where  $T = 25^\circ\text{C}$  and the bottom plate is set to  $T = 40^\circ\text{C}$ . Fig. 5.4(b) shows the mean streamwise temperature profile obtained by spatially averaging in the spanwise direction. The thermal jump is considered a sharp thermal interface with a thermal gradient of  $450^\circ\text{C}$  per meter ( $0.45^\circ\text{C}/\text{mm}$ ), which is greater than that investigated by Moretti *et al.* [?]. Note that the temperature of the insulating region separating the plates cannot be accurately determined from the IR images owing to the difference in emissivity between the insulated region and the convective plate. The embedded thermocouples show the temperature difference between the two plates to be  $15^\circ\text{C}$ .

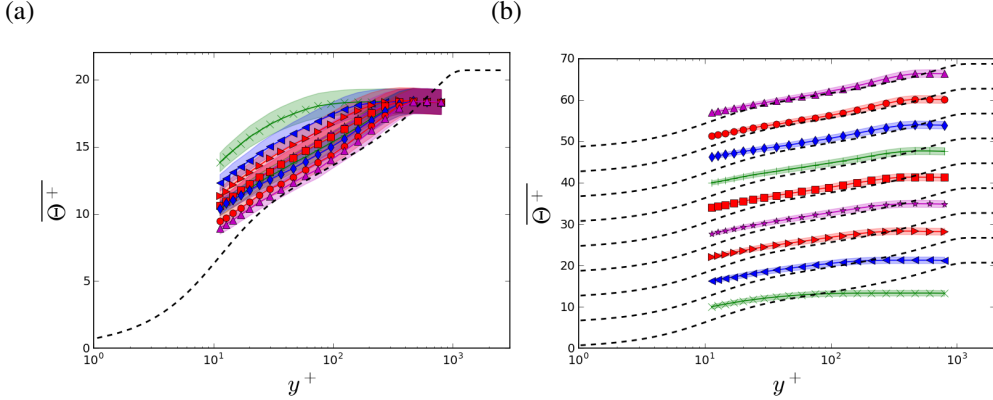


**Figure 5.5.** Wall-normal profiles of mean temperature after thermal step. Plates heated corresponding to profiles is as follows; #9  $\times$ , #8-9  $\blacktriangleleft$ , #7-9  $\blacktriangleright$ , #6-9  $\star$ , #5-9  $\blacksquare$ , #4-9  $\textcolor{green}{+}$ , #3-9  $\blacklozenge$ , #2-9  $\bullet$ , #1-9  $\blacktriangle$ . Plotted in (a) inner-coordinates using  $St$  (Eq. 2.2), and (b) modified inner-coordinates using  $St_T$  (Eq. 5.2), subsequent profiles are offset by  $\Theta^+ = 6$  for visual clarity. The dotted line denotes the law of the wall turbulent profile.

The wall-normal ( $y$ -direction) mean temperature profile was obtained by time averaging the thermocouple signal at a given  $y$ -position over a record length of 100 seconds ( $\approx 1000\delta/u_\tau$ ). Fig. 5.5 shows the mean temperature profiles plotted in outer and inner coordinates for the nine different unheated starting lengths. Owing to the difficulty of evaluating  $\delta_T$  for short thermal development lengths (i.e, large  $x_T$  with fixed profile measurement location), the so-called thermal displacement thickness given by

$$\delta_T^* = \int_0^\infty \frac{T(y) - T_\infty}{T_w - T_\infty} dy, \quad (5.1)$$

was used for outer normalization [?]. The wall heat flux values used for inner-normalization is determined from the correlation

$$St(x) = St_T \left[ 1 - \left( \frac{x_T}{x} \right)^{9/10} \right]^{-1/9} \quad (5.2)$$

developed by [?] as as an approximate solution for the heat transfer downstream of a wall temperature step in a ZPG boundary layer flow, where  $St_T$  is given by Eq. 2.2 and  $x_T$  is the unheated starting length. The profiles (each shifted by  $\Theta^+ = 6$ ) show approximate collapse on the expected

turbulent profile (dashed lines in the figure) that improves with decreasing  $x_T$ . These datasets demonstrate that the flow over the plate encountering a wall temperature step is consistent with previous studies [?, ?], validating the ability of the thermal wall plate to produce temperature step wall boundary conditions.

### ZPG turbulent boundary layer flow around a wall mounted hemisphere body

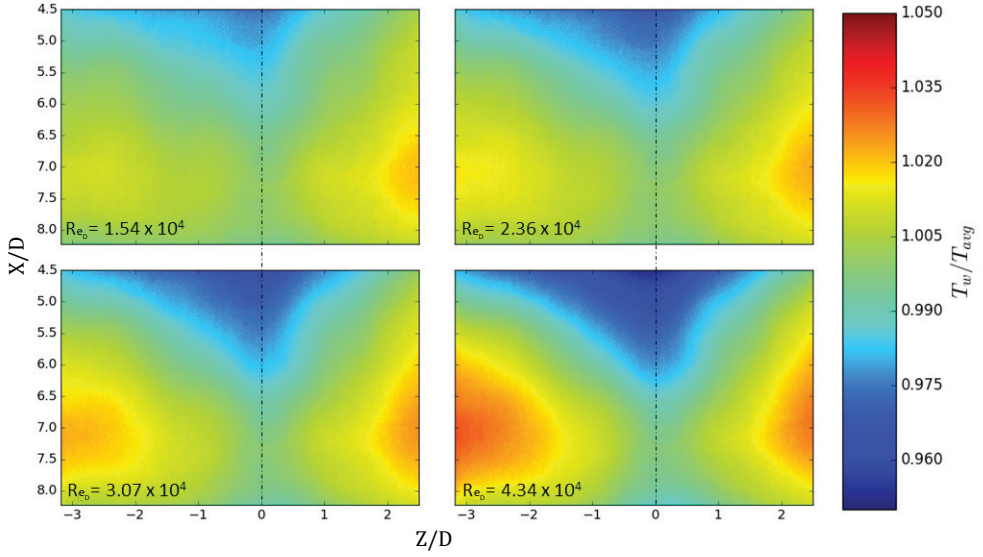


**Figure 5.6.** Spatial temperature distributions located downstream of a hemisphere for four values of  $Re_D$ . The streamwise and spanwise positions have been normalized by the hemisphere diameter  $D = 3\text{cm}$ .

When a boundary layer flow encounters a wall-mounted hemisphere body, the pressure gradients around the hemisphere lead to the formation of a necklace vortex at the hemisphere base with legs that extend downstream [?]. Flow separation at the top of the hemisphere produces vortex loops in the near-wake region [?, ?]. The vorticity in far wake structure is comprised of both the necklace vortex and the vortex loops (see Fig. 5.7). The influence of these types of fluid-structure interactions on heat transfer are important across a broad range of problems from flow over glaciers to atmospheric re-entry vehicles.

In the present study, a wall mounted hemisphere body of diameter  $D = 3\text{cm}$  was placed on the leading edge nose just upstream of the first convective wall plate. The boundary layer upstream of the hemisphere is laminar and the boundary layer is thin compared to the hemisphere with  $\delta/D \approx 0.1$ . The set point temperature of the convective wall plate was  $60^\circ\text{C}$ . The inlet air was unheated with  $T_\infty = 23^\circ\text{C}$ . IR images of the thermal wall plate were acquired downstream of the hemisphere with an imaged area from  $4.5 \lesssim X/D \lesssim 8.2$  (i.e., near the trailing edge of the first conductive wall plate) and from  $-3.0 \lesssim Z/D \lesssim 2.5$ , where  $Z/D = 0$  denotes the centerline of the hemisphere in the streamwise direction. Ensemble-averaged IR images of the spatial distribution of the wall plate temperature at four values of  $Re_D$  are shown in Fig. 5.6. The colormap corresponds to the plate temperature normalized by the average temperature of the plate.

The spatial distribution of temperature in the IR images show a distinct pattern that becomes more pronounced with increasing  $Re_D$ . The spatial pattern of temperature indicates that wake vorticity carries cold freestream fluid towards the wall near the plane of symmetry (i.e. near  $Z/D = 0$  in the figure). The tapered pattern of minimum temperature (maximum heat transfer) is consistent with the study of [?] where local mass (heat) transfer measurements were acquired using naphthalene sublimation that showed a similar tapered shape and that the maximum heat transfer occurred near the reattachment point (which is likely upstream the measurement field-of-view near  $X/D \approx 2.5$ .) The high temperature lopes in the pattern likely result from the spanwise motion of high temperature fluid along the wall (see Fig. 5.7 plane view). Moreover, the center of the lope is likely a signature of the vortex structure driving the spanwise motion.

While the pattern observed in Fig. 5.6 is interesting and informative of the flow structure above the plate, it is evident that the wall-plate temperature is not constant as desired but varies by approximately  $\pm 5\%$  across the convective plate. The difficulty of course is that large spatial variations in the convective heat transfer coefficient exist across the convective plate owing to the strong three dimensionality of the flow behind the hemisphere. Since the design purpose was to set and hold fixed the convective wall plate temperature at a desired temperature, the design needed to be modified. This was accomplished by first replacing each of the two center thin film resistive heaters by

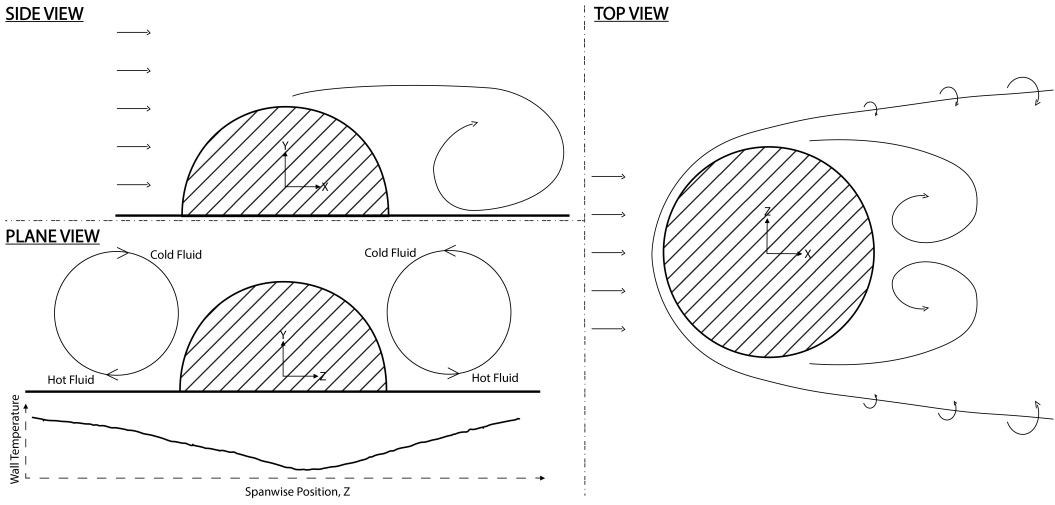


**Figure 5.7.** Two plane view of cartoon depiction for resulting flow field from hemisphere perturbation. The XZ plane provides a birds eye view of the developing vortex wake, and the YZ plane provides a view of vortex wake downstream of the hemisphere and the resulting wall temperature.

two heaters of half the original size, now giving 4 separate heaters in the middle section of the convective plate. Next, the number of controllers was increased from one to two, one for each half of the convective plate. Then the number of controllers was increased from two to three controllers, where the center controller was used for the center two resistive heaters and the remaining two controllers were used for the left and right section of the plate. The mean spanwise temperature profile obtained by spatially averaging in the streamwise direction is shown in Fig. 5.8 for each control scheme at  $Re_D = 2.4 \times 10^4$ .

The profiles for two and three controllers shows that the spatial variation is further reduced by increasing the number of independent controllers. By using three controllers, the spatial variation of temperature is within  $\pm 1\%$  which is less than the measurement uncertainty of the IR temperature measurement. Given this lack of resolution it is difficult to assess the apparent asymmetry in the profiles but a reasonable assumption is that the asymmetry is likely due to somewhat different responses of the left and right controller. In brief, these results demonstrate the ability of the

thermal wall plate design to be easily adjusted to maintain a nearly uniform wall temperature in a highly three-dimensional flow.

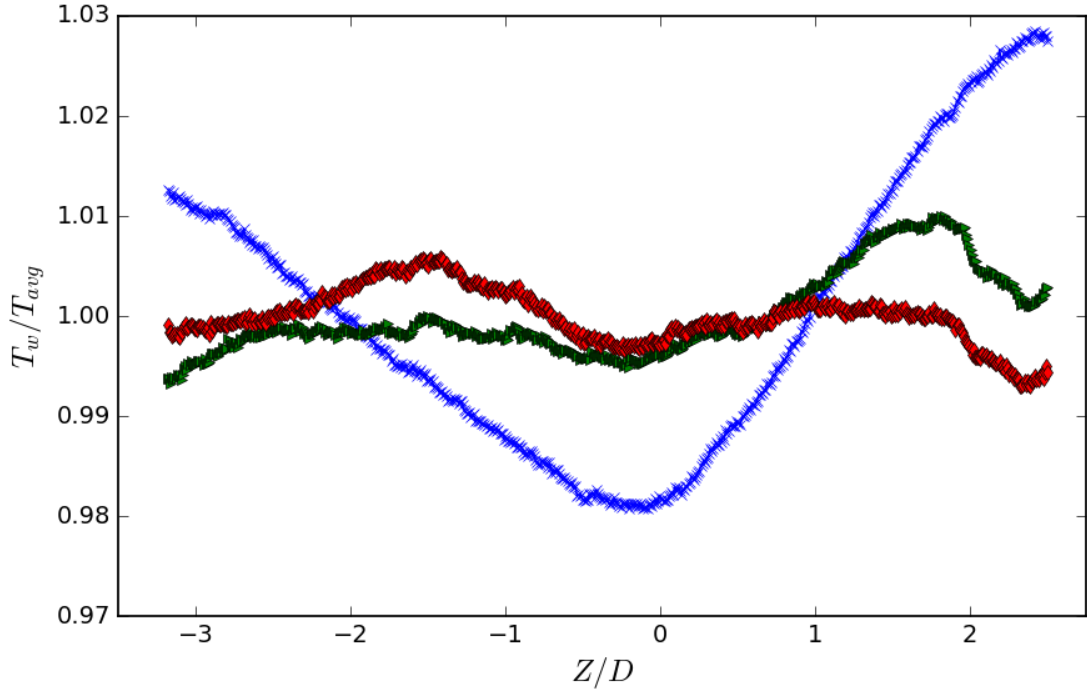


**Figure 5.8.** Spanwise temperature profiles taken from the center of the IR images at a downstream position of 1 controller,  $\text{X}$ ; 2 controllers,  $\blacktriangleright$ ; 3 controllers,  $\diamond$

## Non-equilibrium Flow

## Modified Correlations

## **CHAPTER 6**

## **CONCLUSION**

## **BIBLIOGRAPHY**

## **APPENDIX A**

## **DRAWINGS**

Some sweet pictures!

... . . .

## APPENDIX B

### COMPONENTS

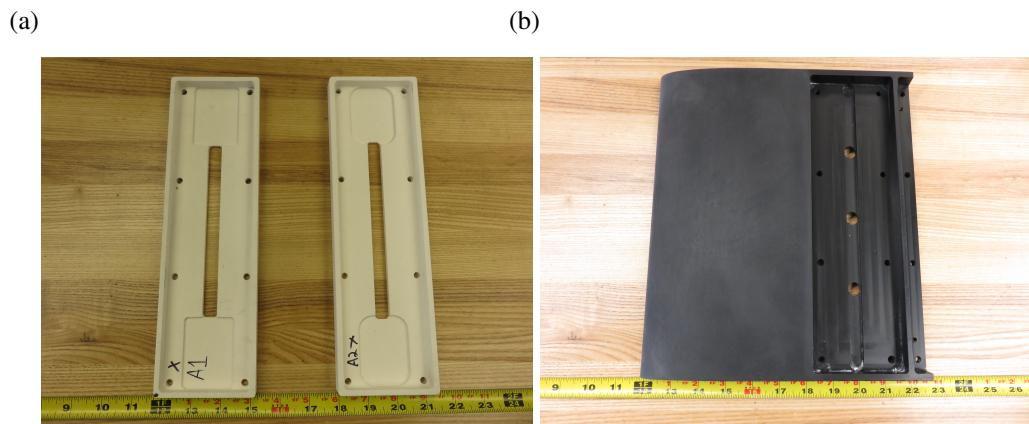


**Figure B.1.** (a) insulation (b) frame.

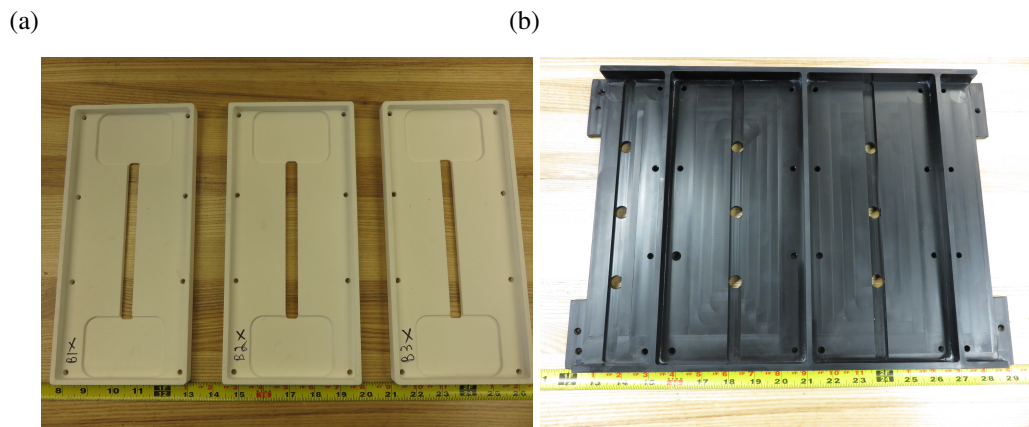


**Figure B.2.** (a) insulation (b) frame.

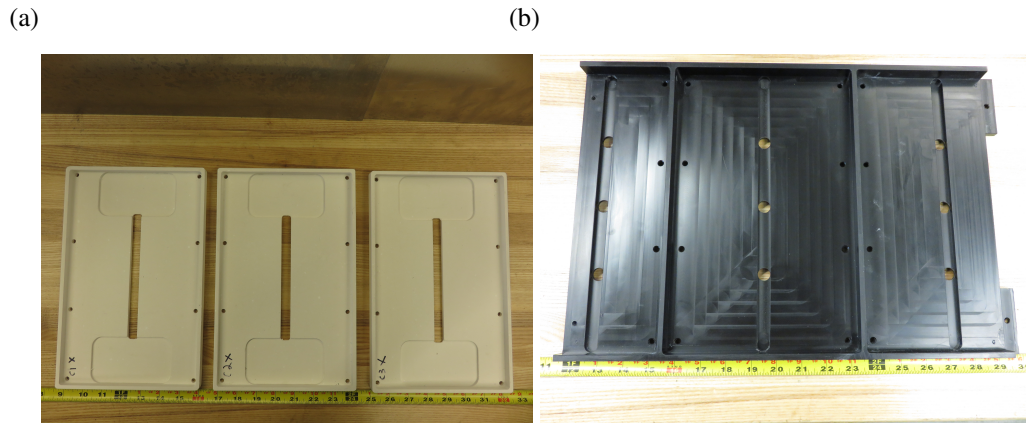


**Figure B.3.** (a) insulation (b) frame.

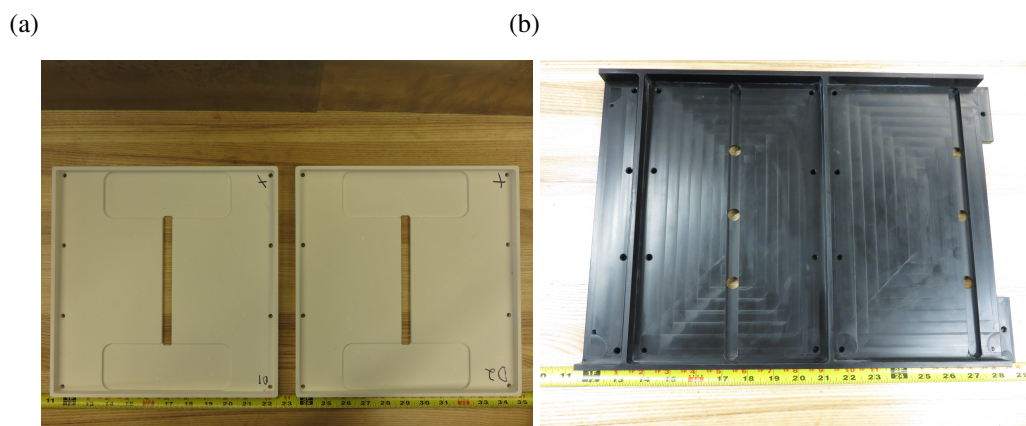


**Figure B.4.** (a) insulation (b) frame.

(a)

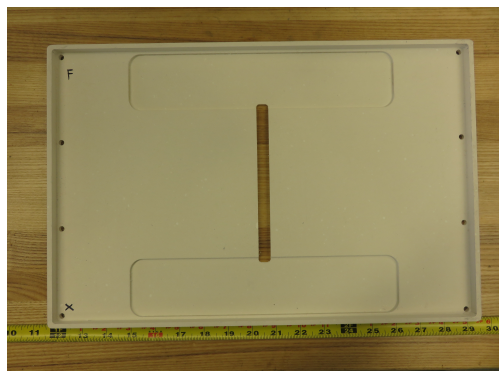


(b)



**Figure B.5.** (a) insulation (b) frame.

(a)



(b)



**Figure B.6.** (a) insulation (b) frame.

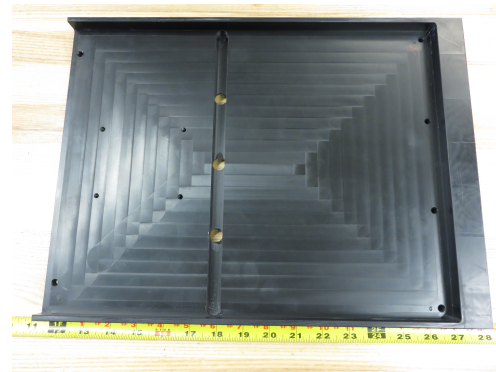


**Figure B.7.** part

## **APPENDIX C**

### **MORE EXTRA STUFF**

This is another appendix.